



# High Spatial Resolution mapping of Precipitable Water Vapor using SAR interferograms, GPS observations and ERA-Interim reanalysis

W. Tang<sup>1</sup>, M. S. Liao<sup>1,2</sup>, and L. Zhang<sup>1</sup>, W. Li<sup>3</sup>, W. M. Yu<sup>4</sup>

<sup>1</sup>State Key Laboratory of Information Engineering in Surveying, Mapping and Remote Sensing, Wuhan University, Wuhan, 430079, China

<sup>2</sup>Collaborative Innovation Center for Geospatial Technology, Wuhan University, Wuhan, 430079, China

<sup>3</sup>Shanghai Institute of Satellite Engineering, Shanghai, 201100, China

<sup>4</sup>Shanghai Academy of Spaceflight Technology, Shanghai, 201100, China

Correspondence to: L. Zhang (luzhang@whu.edu.cn)

**Abstract.** A high spatial resolution of the Precipitable Water Vapor (PWV) in the atmosphere is a key requirement for the short-scale weather forecasting and climate research. The aim of this work is to derive temporally-differenced maps of the spatial distribution of PWV by analyzing the atmospheric delay “noise” in Interferometric Synthetic Aperture Radar (InSAR). A time series maps of differential PWV were obtained by processing a set of ENVISAT ASAR images cover the area of Southern California, USA from 06 October 2007 to 29 November 2008. To get a more accurate PWV, the component of dry delay is calculated by using ERA-Interim reanalysis products. In addition, the ERA-Interim was used to compute the conversion factors required to convert the zenith wet delay to water vapor. The InSAR-derived differential PWV maps were calibrated by means of the GPS PWV measurements over the study area. We validated our results against the measurements of PWV derived from the MEdium Resolution Imaging Spectrometer (MERIS) which is located together with ASAR sensor onboard the ENVISAT satellite. Our comparative results show strong spatial correlations between the two data sets. The difference maps have Gaussian distributions with mean values close to zero and standard deviations below 2 mm. The advantages of the InSAR technique is that it provides water vapor distribution with a spatial resolution as fine as 20 m and an accuracy of ~2 mm. Such a high spatial resolution maps of PWV could lead to much greater accuracy in meteorological understanding and quantitative precipitation forecasts.

## 1 Introduction

The performance of Interferometric Synthetic Aperture Radar (InSAR) data when constructing digital elevation models (DEM) or precisely measuring surface deformation of the Earth is limited by the atmospheric delay caused by the water vapor content in the lower part ( $\leq 1.5$  km) of the troposphere (Beauducel et al., 2000; Liao et al., 2013; Zebker et al., 1997). Although the water vapor contributes only about 10% of total atmospheric delay, this source of error is not easily eliminated due to its high spatial and temporal variability. Our aim in this paper is to investigate the atmospheric delay “noise” of InSAR as a meteorological signal to measure the water vapor content in the atmosphere. We will present a new approach for



accurate water vapor constructing with a high spatial resolution by combing InSAR observations, GPS data, and a Global Atmospheric Model (ERA-Interim), and evaluate the performance.

Various techniques have been applied to successive measurement of the horizontal and vertical distributions of water vapor in the atmosphere either from space or ground. Water vapor measurements produced by radiosondes or water vapor radiometers are limited in the spatial and temporal resolution. Global Navigation Satellite Systems (GNSS) provides water vapor measurements with a dense temporal sampling and high accuracy but the GNSS networks are too sparse and irregular to capture fine-scale water vapor fluctuations. The passive multispectral imager such as MEdium Resolution Imaging Spectrometer (MERIS) and Moderate Resolution Imaging Spectroradiometer (MODIS) only produce continuous water vapor maps during day time or under cloud-free weather conditions. These limitations are the main error source in short-term (0-24 hour) precipitation prediction. The advantage of satellite-based InSAR, a relative new tool for water vapor mapping, is that it could provide maps of water vapor with a spatial resolution as fine as 10-20 m over a swath of ground about 100 km wide.

In this paper, we used the InSAR data in combination with GPS measurements and ERA-Interim reanalysis products to precisely estimate the water vapor content in the atmosphere. The main concept of InSAR-based water vapor mapping is that the atmospheric phase delay is considered as our interested signal to be extracted and the other phase components are treated as noise to be removed. The atmospheric phase delay consists of two components: dry delay and wet delay. The dry delay varies with local temperature and atmospheric pressure which is smooth in time and space while the wet delay varies with water vapor partial pressure which is more spatially and temporally varying. Within a typical interferogram area of  $100 \times 100$  km, the pressure usually varies less than 1hPa, while a significant changes of the water vapor partial pressure are common. Consequently, the wet delay in the differential interferogram is much greater than the dry delay. Therefore, most studies have focused on estimating the wet delay and neglected the dry delay. However, recent studies also show that dry delay varies significantly at low elevation and cannot be neglected (Doin et al., 2009; Jolivet et al., 2014). Thus, for accurate water vapor mapping, dry delay in InSAR must be taken into account. In this work, we compute the component of dry delay by using ERA-Interim reanalysis products. Using the water vapor conversion factor, the InSAR-derived zenith wet delay is then mapped onto Precipitable Water Vapor (PWV), a quantity representing the water vapor content in the atmosphere. In this study, the outputs of temperature and specific humidity from ERA-Interim model are used to estimate this water vapor conversion factor. It should be noted that water vapor maps from InSAR are derived from the difference between the water vapor variations during two Synthetic Aperture Radar (SAR) images with a temporal separation of one or more days, we call  $\Delta$ PWV hereafter. The temporal interval relies on the space-borne InSAR mission: 1 day (tandem ERS-1/2), 11 days (TerraSAR-X, Cosmo-SkyMed), 12 days (Sentinel-1), 35 days (ENVISAT-ASAR, RADARSAT) and 46 days (ALOS-PALSAR). The main problem of this operation is that the  $\Delta$ PWV maps is a relative measurement and requires absolute observations to calibrate each  $\Delta$ PWV map. The calibration procedure was implemented by using absolute measurements of PWV from a few GPS stations in our study area. After that, the accuracy of the calibrated  $\Delta$ PWV maps were evaluated by



comparing with the  $\Delta$ PWV from the collocated GPS stations. Finally, we made a comparative analysis of  $\Delta$ PWV maps from InSAR and MERIS pixel by pixel, and by inspecting the spatial properties.

## 2 Study area and data sets

We carried out the study using data sets collected in the Los Angeles basin located in Southern California, USA. This study area neighbours the Pacific Ocean in the west and southwest and thus is rich with atmospheric water vapor and it is well covered by a dense network of continuous GPS receivers. These conditions make it particularly suitable for atmospheric water vapor studies. Figure 1 shows the topography map of the study area. A set of  $N=8$  ENVISAT ASAR mages were acquired over this region for the period between 06 October 2007 to 29 November 2008. The images were acquired during descending passes, Track 170, with the look angle  $\theta = 22.6^\circ$ . The acquisition time was 18:01 UTC. For SAR interferometric processing, an external DEM with 30 m height postings from Shuttle Radar Topography Mission (SRTM) was used for removing the influence of topography and the Earth's curvature, while the precise orbit information from Delft Institute for Earth-Oriented Space Research was utilized for minimizing the orbital errors. The black square in Fig.1 shows the footprint of SAR images.

We used 29 permanent GPS stations in the Southern California Integrated GPS Network (SCIGN) within the SAR image scene to estimate atmospheric water vapor over Southern California. SCIGN is one of densest GPS network in the world, with more than 250 continuously operated GPS stations. Most of the GPS stations of SCIGN have been integrated into the Plate Boundary Observatory (PBO) in 2008. PBO has two GPS Analysis Centers (ACs) that process raw GPS data and produces position solutions for stations in the PBO network as well as selected other stations. One AC is operated by the Geodesy Laboratory at Central Washington University (CWU) and uses the GIPSY/OASIS-II processing package. The other AC is located at the New Mexico Institute of Technology (NMT) and uses GAMIT/GLOBK. The analysis centers provide tropospheric data products including zenith atmospheric delay are archived at the UNA VCO Data Center and are openly and freely available (<http://www.unavco.org/data/data.html>). The availability of GPS measurements also allowed us to separate possible surface deformation from the atmospheric signals in differential interferograms. The red triangles in Fig. 1 represent the locations of GPS stations.

The ERA-Interim reanalysis from European Centre for Medium-Range Weather Forecasts (ECMWF) is used to produce maps of dry delay and water vapor conversion factor. ERA-Interim is a global atmospheric model which was instigated to address some of the problems seen in ERA-40 (Dee et al., 2011). It is based on 4-dimensional variational assimilation of global surface and satellite meteorological data. The outputs of ERA-Interim used in our study are estimates of temperature, specific humidity, and geopotential height, defined at 37 pressure levels (1000–1 hPa), and a spatial resolution of  $0.75^\circ$  (~75 km). The black crosses in in Fig. 1 shows the distribution of ERA-Interim model grid nodes used in this study. The MERIS



is located together with ASAR sensor on board of ENVISAT satellite (Bennartz and Fischer, 2001), thus the simultaneous water vapor measurements from MERIS were used as a reference data for comparison and evaluation.

### 3 Estimating PWV from InSAR

Here, we present the methods for obtaining zenith wet delay from SAR interferogram and converting it to PWV. In Sect.3.1, the retrieval of zenith wet delay from SAR interferogram is described. Section 3.2 describes the method for computing the conversion factor required to map the zenith wet delay onto PWV by using ERA-Interim reanalysis. In Sect.3.2, the approach for calibrating the PWV estimated from InSAR using GPS observations is discussed.

#### 3.1 Atmospheric delay in InSAR

The unwrapped interferometric phase for each pixel in an interferogram is given by the superposition of several components including topography, Earth surface displacement, and atmosphere. It can be written as:

$$\Phi_{int} = \Phi_{topo} + \Phi_{defo} + \Phi_{orb} + \Phi_{atm} + \Phi_{noise} \quad (1)$$

where  $\Phi_{topo}$  is the phase contribution from land topography,  $\Phi_{defo}$  represents the ground deformation between the acquisitions,  $\Phi_{orb}$  counts for the phase caused by inaccurate satellite orbit,  $\Phi_{atm}$  indicates the phase delay caused by atmospheric state variations during SAR acquisitions and  $\Phi_{noise}$  denotes the noise component including system thermal noise, decorrelation noise, co-registration noise and processing noise. The contribution of topography is compensated for by using an external DEM (30 m SRTM DEM are used in this study, Fig. 2a). An example of original unwrapped interferogram (master image-16 August 2008, slave image-25 October 2008) is shown in Fig. 2b, with the topographic phase component subtracted. The orbital error was modeled by a network de-ramping method described in (Jolivet et al., 2011) and estimated separately from the unwrapped phase. A strong, localized, vertical displacement in the Los Angeles Basin areas was observed in a number of interferograms although those interferograms possess short temporal baselines. The rapidly subsiding displacement area in the Los Angeles Basin region was masked out from all interferograms to avoid mixing the atmospheric signal with surface deformation. After subtracting the topographic phase and orbital ramp, the residual phase observations in the unwrapped interferograms only result from the atmospheric delay during SAR acquisitions. This atmospheric delay only contains the delay caused by neutral atmosphere because the ionospheric effects are negligible in the C-band SAR signal we used in this study (Hanssen, 2001). The atmospheric phase delay  $\Phi_{atm}$  can be classified into dry and wet components.

$$\Phi_{atm} = \Phi_{dry} + \Phi_{wet} \quad (2)$$

where

$$\Phi_{dry} = -\frac{4\pi}{\lambda \cos \theta_{inc}} 10^{-6} \left[ \frac{k_1 R_d}{g_0} (P(z) - P(z_0)) \right] \quad (3)$$

$$\Phi_{wet} = -\frac{4\pi}{\lambda \cos \theta_{inc}} 10^{-6} \int_{z_0}^{z_{ref}} \left[ \left( k_2 - \frac{R_d}{R_v} k_1 \right) \frac{e}{T} + k_3 \frac{e}{T^2} \right] dz \quad (4)$$



The dry delay is calculated using the specific gas constant for dry air  $R_d$ , gravity acceleration at ground level  $g_0$ , and air pressure  $P$ . The wet delay is computed using the partial pressure of water vapor  $e$ , water vapor specific gas constant  $R_v$ , and temperature  $T$ .  $z_0$  is the ground level and  $z_{ref}$  represents a reference height (30 km used in this study) above which the delay is assumed to be nearly unchanged with time. The atmospheric refractivity constants  $k_1$ ,  $k_2$  and  $k_3$  are determined in (Smith and Weintraub, 1953).  $\theta_{inc}$  is the radar incidence angle and the factor  $\frac{1}{\sin \theta_{inc}}$  is a mapping function applied to project the delay from the zenith direction to the radar line-of-sight (LOS). The constants in Eqs. (3) and (4) are listed in Table 2.

The dry component of atmospheric delay depends on the variations of the atmospheric pressure. This pressure at a given altitude changes over time, even if small, can reach to the total pressure of a few percent, resulting the difference of dry delay to a few centimeters. Moreover, the changes of terrain height introduce a spatial gradient in the atmospheric pressure across the SAR scene, which will cause a small variation in the dry delay (Mateus et al., 2013b). The variation of dry delay depending on the topography could be up to 15 mm in our study area. Therefore, in order to accurately derive the wet delay, the dry delay must be precisely estimated and subtracted from the total atmospheric delay. This delay can be calculated if the atmospheric pressure is known along the signal propagation path or along the zenith direction. In this work, the vertical profiles of atmospheric pressure were extracted from ERA-Interim reanalysis products at the model grid points. We interpolated the atmospheric pressure onto altitude profiles at each model grids using a spline interpolation and calculated the dry delay using Eq. (3). The resulting vertical profiles of dry delay were horizontally interpolated to the resolution of SAR interferogram using a bilinear interpolation. We also used the outputs of temperature and relative humidity from ERA-Interim to produce the maps of water vapor conversion factor using the same interpolation strategy; this will be discussed in next subsection. The map of dry delay is displayed in Fig. 2c, this delay represents a long-wavelength signal and is smooth in space, rose up to 1 cm on the mountain areas. The slant wet delay (Fig. 2d) was obtained by subtracting the dry delay from the total atmospheric delay. The slant wet component of phase delay in LOS was converted to the Zenith Wet Delay (ZWD) in millimeter using a simple mapping function:

$$ZWD_{InSAR} = -\frac{\lambda \cos \theta_{inc}}{4\pi} \phi_{wet} \quad (5)$$

### 3.2 Conversion of ZWD into PWV

The zenith wet delay is considered as a measurement of the water vapor content in the atmosphere. The relationship between the ZWD and PWV can be expressed as (Bevis et al., 1994):

$$PWV = \Pi \times ZWD \quad \text{or} \quad ZWD = \kappa \times PWV \quad (6)$$

where  $\Pi$  is the water vapor conversion factor and  $\kappa = \Pi^{-1}$  is calculated by the following equation.

$$\kappa = 10^{-6} \rho R_v \left( \frac{k_3}{T_m} + k_2 - w k_1 \right) \quad (7)$$



where  $\rho$  is the density of the liquid water (listed in Table 2) and  $w$  ( $\sim 0.668$ ) is the mass ratio of water vapor molecule to dry air molecule.  $T_m$  is the weighted mean temperature of the atmosphere and it is related to the surface temperature  $T_s$  in degrees Kelvin (Bevis et al., 1992).

$$T_m = 70.2 + 0.72 \times T_s \quad (8)$$

5

Using this relationship to estimate  $T_m$  will produce approximately 2% error in PWV (Bevis et al., 1992). The most accurate way to compute the mean temperature is to calculate the following integral equation between the ground surface  $z_0$  and the reference height  $z_{ref}$ , given by (Davis et al., 1985),

$$T_m = \frac{\int_{z_0}^{z_{ref}} (e/T) dz}{\int_{z_0}^{z_{ref}} (e/T^2) dz} \quad (9)$$

10

The value of  $\kappa$  is dimensionless and usually ranges from 6.0 to 6.5 (and could be up to 7.0 at some circumstances) (Bevis et al., 1992). For the purpose of rough conversion between ZWD and PWV, an empirical constant  $\kappa = 6.25$  ( $\Pi = 0.16$ ) was used. However, the actual value of  $\Pi$  changes with water vapor pressure and temperature that minor errors in  $\Pi$  could result in significant biases in PWV. For example, using the constant value  $\Pi = 0.16$  and assuming the ZWD as 200 mm, the corresponding value of PWV is 32 mm. However, if the value of  $\Pi$  is computed using Eqs. (7) and (9) as 0.15, then the value of PWV will be 30 mm. In fact, the larger the ZWD, the more critical is the value of  $\Pi$ . Rather than using the empirical constant value, we evaluated the conversion factor  $\Pi$  at each pixel of the SAR interferogram using ERA-Interim reanalysis. To compute the weighted mean temperature  $T_m$ , the outputs of ERA-Interim we used are the vertical profiles of temperature and relative humidity. The relative humidity is converted to partial pressure of water vapor  $e$  by a mixed Clausius-Clapeyron law (Jolivet et al., 2011). To evaluate the sensitivity of  $\kappa$  to the weighted mean temperature  $T_m$ , its values are computed over 120 days (10 days in one month) in the year of 2007 and 2008. Figure 3 plots  $\kappa$  against  $T_m$  that is estimated using outputs of  $e$  and  $T$  from the three ERA-Interim model grids (indicated as the black crosses in Fig. 1) located within the SAR scene. From Fig. 3, we observed that the value of  $\kappa$  changes with  $T_m$ , and  $\kappa$  is in the range of 6.09 to 6.79 in the year of 2007 (Fig. 3a), whereas it varies between 6.17 and 6.74 in the year of 2008 (Fig. 3b). The fitted average curves linearly decrease with rates of  $-0.0214/\text{K}$  and  $-0.0221/\text{K}$ , respectively. As expected that the value of  $\kappa$  is much higher on winter days (low temperature) than on summer days (high temperature). On the other hand, since the temperature generally decreases with altitude in the troposphere, the conversion factor is correlated with the elevation. Therefore, using the empirical value of  $\Pi = 0.16$  is not appropriate for our study area; rather its value is calculated using global atmospheric model ERA-Interim. Figure 4 shows the spatial distribution map of  $\kappa$  on 16 August 2008 produced by ERA-Interim. It can be seen that the value of  $\kappa$  varies spatially and it has a higher value on the mountainous areas than those areas with a flat terrain.



### 3.3 InSAR PWV calibrated by GPS PWV

The temporal differences of PWV ( $\Delta$ PWV) estimated by InSAR and GPS are not directly comparable. The unwrapping procedure introduces an arbitrary constant in the unwrapped phase, so the InSAR technique can just measure the  $\Delta$ PWV as a relative measurement whereas the GPS-based  $\Delta$ PWV is an absolute value. To resolve this problem,  $\Delta$ PWV maps derived from InSAR are calibrated by GPS-based  $\Delta$ PWV. It should be noted that only the signals from satellites with elevation angle larger than the cutoff elevation angle are recorded by the GPS receiver, thus the GPS PWV represents an average measurement of a reversed cone of the troposphere above the GPS receiver. All observations outside this cone are discarded. Figure 5 shows the schematic diagram of this effect. The cutoff elevation angle is set to  $15^\circ$  and assumes the water vapor concentrated in the lower part (1.4 km) of the troposphere, the corresponding cone radius is approximately 5.4 km. We averaged the  $\Delta$ PWV values of the interferogram pixels located within the corresponding circular area before comparing InSAR measurements to that of GPS. We calculated the temporal difference of the PWV at each GPS station, at about the same acquisition time of the two interferometric SAR images. The InSAR  $\Delta$ PWV calibration process is to determine the constant  $K$  by minimizing the following cost function (Mateus et al., 2013a).

$$\sum_{k=1}^{N_{\text{GPS}}} \left\{ \Delta \text{PWV}_k^{\text{GPS}} - \frac{1}{N_p(k)} \sum_{i=1}^{N_p(k)} \Delta \text{PWV}_i^{\text{InSAR}} + K \right\}^2 \quad (10)$$

where  $N_{\text{GPS}}$  is the number of GPS receivers,  $N_p(k)$  is the number of InSAR pixels located within the circular area around the  $k$ th GPS receiver,  $\Delta \text{PWV}_k^{\text{GPS}}$  is the temporal difference of PWV between master and slave dates by GPS,  $\Delta \text{PWV}_i^{\text{InSAR}}$  represents the  $\Delta$ PWV estimated by InSAR. Finally, the relative map of the  $\Delta$ PWV in interferograms were calibrated by adding the constant  $K$  to  $\Delta \text{PWV}^{\text{InSAR}}$  map.

## 4 Results and discussion

In this section, we will evaluate and validate the performance of InSAR-based water vapor mapping by comparing the calibrated  $\Delta$ PWV estimated from InSAR to  $\Delta$ PWV measurements from GPS, as well as measured values from MERIS. The evaluation was conducted as follows. PWV measurements at each GPS station were compared to PWV from MERIS. This comparison is important since possible errors in the GPS PWV can be detected by comparing to MERIS PWV, a relatively high accuracy retrieval of water vapor. The calibrated  $\Delta$ PWV maps of InSAR are compared to the absolute value of  $\Delta$ PWV at each GPS station. This comparison helps to check the orbital errors due to the inaccurate satellite ephemeris and to verify that the unwrapped phase is only due to tropospheric delay and not to the earth surface displacement. The last step is to compare the calibrated InSAR time series maps of  $\Delta$ PWV to the MERIS water vapor maps on a pixel-wise basis. In such a way, it is possible to cross validate the accuracy of water vapor measurements from the two techniques and also inspect their spatial distribution properties.



#### 4.1 GPS PWV measurements

The tropospheric products analyzed by CWU on the 29 GPS stations (Fig. 1) are used in this study. These products provide the zenith atmospheric delay at each GPS stations every 5 minutes. The high temporal sampling of GPS measurements makes us enable to obtain the zenith wet delay at a time as close as possible to the SAR images acquisition time. The cutoff elevation angle ( $\theta_{\text{cut}} = 15^\circ$ ) was accepted in this study. The Saastamoinen model and gridded Vienna Mapping Function (VMF1GRID) (Kouba, 2007) were used for calculating a priori values of zenith dry delay. The zenith wet delay was then obtained by subtracting the zenith dry delay from the total delay. The zenith wet delay was finally mapped onto PWV using the water vapor conversion factor estimated from ERA-Interim reanalysis products.

10 As an example of the GPS PWV, Fig. 6 displays the 24-hour time series of the PWV estimated from GPS observations at 29 stations on 15 December 2007 (winter), 03 May 2008 (spring), 16 August 2008 (summer) and 25 October 2008 (autumn), four of the SAR acquisition days in our study. In summer, high temperature causes water to evaporate from the surface of lakes and oceans, resulting in higher PWV content and more variable, whereas in autumn and winter, the lower and smoother PWV were observed due to dry weather conditions.

15

In Fig. 7, we plot PWV measurements derived from MERIS against PWV results estimated from GPS at 29 stations on the four SAR acquisition days (in Fig. 6). Since GPS PWV estimates represent average values over the reversed cone with a  $\sim 5.4$  km radius base, we averaged the PWV from MERIS within the circular area around the location of the GPS stations. The result shows a strong correlation (0.95) between GPS and MERIS. The mean absolute error (MAE) of the differences between the two data sets does not exceed 0.5 mm and the root mean square (RMS) value is 0.60 mm. The slope of the line in Fig. 7 is 0.98. Thus GPS and MERIS measurements of water vapor are in a good agreement as we should not expect a perfect correlation between the two data sets because we averaged the conical effect of GPS with a circle and there is noise in both data sets.

20

#### 4.2 InSAR $\Delta$ PWV measurements

25 The eight ENVISAT ASAR images are used for interferometric processing. The constraints for normal baseline ( $< 300$  m) and temporal baseline ( $< 105$  days) are used in order to minimize the effects of ground deformation and decorrelation noise. We used the DORIS software for interferogram formation. Table 1 summarizes the baseline information and the height ambiguity for all of the interferograms. The height ambiguity is defined as the altitude difference that generates an interferometric phase change of  $2\pi$  after interferogram flattening. In principle, the smaller value of the height ambiguity, the lesser sensitivity of the interferometric phase to the possible errors in the external DEM. Small values of height ambiguity ensures that interferometric phase is primarily related to atmospheric delay. Adaptive power spectrum filter has been applied to interferograms to reduce phase noise. All interferograms were multilooked by 40 looks in azimuth and 8 looks in range to

30



enhance the coherence quality and improve the phase unwrapping accuracy. The multilook processing resulted in a reduction of the spatial resolution of the interferograms to  $160 \times 160$  m. The wrapped phases were unwrapped using a branch cut algorithm (Goldstein et al., 1988) and possible orbital errors were corrected by network de-ramping method. The local rapid ground subsiding region and significant decorrelation areas were masked out. The wet delay differences of InSAR were obtained by subtracting the component of dry delay predicted from ERA-Interim. The wet delay differences were mapped onto  $\Delta$ PWV maps using the water vapor conversion factor as explained in Sect. 3.2.

Due to the fact that the unwrapped processing introduced an arbitrary constant into the phase, all the  $\Delta$ PWV maps from InSAR were relative measurements and were calibrated to absolute value by using the PWV from GPS. The GPS PWV values were estimated from the zenith wet delay provided by the CWU data analysis center as described in previous section. The overpass time of ENVISAT satellite was 18:01 UTC, thus we computed the temporal difference of the PWV at each GPS station at time 18:00 UTC, making the time differences negligible. Using the  $\Delta$ PWV estimates from GPS, the  $\Delta$ PWV maps of InSAR were calibrated by solving the cost function (Eq. (10)) as described in Sect. 3.3. A comparison of the calibrated  $\Delta$ PWV from the interferogram (master image-16 August 2008, slave image-25 October 2008, see Fig. 2) and  $\Delta$ PWV from the 29 GPS stations is displayed in Fig. 8a. The slope of the line in this figure is 0.73 while the correlation coefficient is 0.95, suggesting the GPS and InSAR measurements of PWV are in reasonable agreement although there is noise in both data sets. Figure 8b plots the  $\Delta$ PWV from GPS and InSAR as a function of elevation. This plot shows that the content of water vapor depends on the altitude and decreases as the altitude increases. The GPS site WLSN has the highest elevation among all GPS stations, so it shows the lowest water vapor content. The global negative correlation between  $\Delta$ PWV and altitude (Fig. 8b) implies that the absolute humidity in the bottom layer of atmosphere was smaller at the acquisition time of the slave image than at the acquisition time of the master image. The quantitative comparison of this interferogram is summarized in Table 3. It can be seen that most of differences are smaller than 2 mm. The MAE of  $\Delta$ PWV between GPS and InSAR is 0.70 mm and the RMS value is 0.91 mm. It is worth noting that, large differences between InSAR and GPS at stations CGDM, ECFS and WLSN (indicated by the black arrows in Fig. 8) were observed, especially the largest difference (-2.84 mm) at station WLSN. The standard deviations of InSAR pixels located within the circular area around these three GPS stations also show a high value (the fourth column in Table 3). The three GPS stations are located in mountain areas with an altitude 730, 820, 1700 meters for the CGDM, ECFS and WLSN stations, respectively. This interferogram also show a high value for height ambiguity (290.90 m). Therefore, we can conclude that the large discrepancies between InSAR and GPS for these three stations are due to the topographic phase error during interferometric processing.

The comparisons of  $\Delta$ PWV from the two techniques at each GPS station for the ten interferograms are shown in Fig. 9. A good agreement between the InSAR and GPS was found in the whole data sets. Large differences between InSAR and GPS at stations CGDM, ECFS and WLSN were also found on those interferograms with a high value of height ambiguity



(interferograms 1, 2, 4 and 7 in Table 1). The PWV estimates from the two techniques characterized by different sampling properties both in space and time. GPS can provide an absolute value of the PWV every five minutes but refers to the parts of atmosphere observed within a cone whose radius depends on the elevation cutoff angle, whereas InSAR gives a high spatial resolution map of the  $\Delta$ PWV with a time separation of 35 days or more. The high temporal sampling of GPS and high spatial resolution of InSAR are complementary for numerical weather modeling, which will improve the model resolution and give a better understanding of the structure of atmospheric patterns.

#### 4.3 Validation using water vapor measurements from MERIS

In this section, we will evaluate and analyze the accuracy of time series of the calibrated  $\Delta$ PWV maps derived from InSAR to confirm the performance of this technique as a tool for water vapor mapping. We carry out a cross-validation pixel by pixel using cloud-free water vapor measurements from MERIS acquired simultaneously with the ENVISAT ASAR images. The water vapor content is expressed as integrated water vapor (IWV) in the MERIS products. The theoretical accuracy of the MERIS IWV under cloud-free conditions over land is  $0.16 \text{ g m}^{-2}$  at full resolution ( $\sim 300 \text{ m}$ ), which corresponds to 1.6 mm accuracy in PWV. This accuracy will deteriorate under cloudy conditions or over water surfaces. The percentage of cloud-free conditions for MERIS data we used in this study are larger than 90% except for the image acquired on 29 November 2008 having a coverage percentage of 80%. For the sake of comparison, we built differences of PWV maps ( $\Delta$ PWV) from MERIS. In Fig. 10, are shown the calibrated  $\Delta$ PWV maps derived from the ten interferograms (in Table 1) and the corresponding  $\Delta$ PWV maps from MERIS data. The first column shows the  $\Delta$ PWV derived from InSAR that have been calibrated with GPS observations. The  $\Delta$ PWV from MERIS are shown in the second column. The third column shows the scatter plot of  $\Delta$ PWV with InSAR on the abscissa and MERIS on the ordinate scale. The histogram of the frequency distributions of the differences between InSAR and MERIS are shown in the fourth column. For all images, the correlation coefficients (Corr) between InSAR and MERIS are computed as well as the root mean square (RMS), mean ( $\mu$ ), and standard deviation ( $\sigma$ ) of the differences between the two data sets. From visual comparison, InSAR  $\Delta$ PWV and MERIS  $\Delta$ PWV show a large spatial correspondence. Furthermore, the quantitative comparisons indicate high correlation coefficients (Corr>0.7) between the two data sets, except for interferogram 3 (master image-15 December 2007, slave image-19 January 2008) and interferogram 9 (master image-16 August 2008, slave image-29 November 2008) having correlation coefficient of Corr=0.5 and Corr=0.67, respectively. The differences between the InSAR and MERIS maps follow a Gaussian distribution with mean values close to zero and standard deviations less than 2mm.

#### 5 Conclusion

In this paper, we presented the results of the temporal evolution of the PWV over Southern California, USA using SAR interferograms during the period from 06 October 2007 to 29 November 2008. Interferograms were spatially averaged and



spatial resolution was reduced to  $160 \times 160$  m. In order to improve the quality maps of atmospheric water vapor, the dry delay was precisely estimated by using ERA-Interim reanalysis products. We also used the outputs from ERA-Interim to produce maps of the conversion factor for mapping zenith wet delay onto PWV at each pixel in the radar scene. All maps of  $\Delta$ PWV derived from interferograms were calibrated using a network of 29 continuous GPS stations located in the SAR scene.

5 The PWV estimates from InSAR and MERIS show strong agreement with the data from GPS. Since the GPS PWV estimates represent the average of the tropospheric effect within a cone above the receiver, InSAR and MERIS pixels were aggregated to enable a proper comparison. The comparative analysis between InSAR and MERIS  $\Delta$ PWV maps demonstrate strong spatial correlation with a less than 2 mm standard deviation for the difference. Our study demonstrates that satellite radar interferometry can be applied to study the spatial distribution of the PWV with a spatial resolution of 20 m and an accuracy

10 of  $\sim 2$  mm. This advantage of InSAR provides unsurpassed insights in capturing the small-scale water vapor distribution. This property could be important for numerical weather forecasting models. Furthermore, forecasting models could take advantage of this source of water vapor maps to enhance the accuracy of their assimilation systems. In turn, the more accurate atmospheric prediction models can be used to correct the atmospheric delay affected by water vapor in the application of geodesy.

15

## Acknowledgements

The authors thank ESA for the ENVISAT ASAR images and MERIS data. The authors would like to thank the GPS data provider: UNAVCO Data Center. This project was supported by the National Natural Science Foundation of China (grant no. 61331016). I would also like to thank Stephen C. McClure for his helpful comments and suggestions on this manuscript.

20

## References

- Beauducel, F., Briole, P., and Froger, J.-L.: Volcano-wide fringes in ERS synthetic aperture radar interferograms of Etna (1992–1998): Deformation or tropospheric effect?, *J. Geophys. Res.*, 105, 16391-16402, 2000.
- Bennartz, R. and Fischer, J.: Retrieval of columnar water vapour over land from backscattered solar radiation using the
- 25 Medium Resolution Imaging Spectrometer, *Remote. Sens. Environ.*, 78, 274-283, 2001.
- Bevis, M., Businger, S., Chiswell, S., Herring, T. A., Anthes, R. A., Rocken, C., and Ware, R. H.: GPS meteorology: Mapping zenith wet delays onto precipitable water, *J. Appl. Meteorol.*, 33, 379-386, 1994.
- Bevis, M., Businger, S., Herring, T. A., Rocken, C., Anthes, R. A., and Ware, R. H.: GPS meteorology : Remote sensing of atmospheric water vapor using the global positioning system, *J. Geophys. Res.*, 97, 15787-15801, 1992.
- 30 Davis, J. L., Herring, T. A., Shapiro, I. I., Rogers, A. E. E., and Elgered, G.: Geodesy by radio interferometry: Effects of atmospheric modeling errors on estimates of baseline length, *Radio. Sci.*, 20, 1593-1607, 1985.



- Dee, D. P., Uppala, S. M., Simmons, A. J., Berrisford, P., Poli, P., Kobayashi, S., Andrae, U., Balmaseda, M. A., Balsamo, G., Bauer, P., Bechtold, P., Beljaars, A. C. M., van de Berg, L., Bidlot, J., Bormann, N., Delsol, C., Dragani, R., Fuentes, M., Geer, A. J., Haimberger, L., Healy, S. B., Hersbach, H., Hólm, E. V., Isaksen, L., Kållberg, P., Köhler, M., Matricardi, M., McNally, A. P., Monge-Sanz, B. M., Morcrette, J. J., Park, B. K., Peubey, C., de Rosnay, P., Tavolato, C., Thépaut, J. N., and Vitart, F.: The ERA-Interim reanalysis: configuration and performance of the data assimilation system, *Q. J. Roy. Meteor. Soc.*, 137, 553-597, 2011.
- Doin, M. P., Lasserre, C., Peltzer, G., Cavalié, O., and Doubre, C.: Corrections of stratified tropospheric delays in SAR interferometry: Validation with global atmospheric models, *J. Appl. Geophys.*, 69, 35-50, 2009.
- Goldstein, R. M., Zebker, H. A., and Werner, C. L.: Satellite radar interferometry: Two-dimensional phase unwrapping, *Radio. Sci.*, 23, 713-720, 1988.
- Hanssen, R. F.: *Radar Interferometry: Data Interpretation and Error Analysis*, 308 pp., Springer, New York, 2001.
- Jolivet, R., Agram, P. S., Lin, N. Y., Simons, M., Doin, M.-P., Peltzer, G., and Li, Z.: Improving InSAR geodesy using Global Atmospheric Models, *J. Geophys. Res.*, 119, 2324-2341, 2014.
- Jolivet, R., Grandin, R., Lasserre, C., Doin, M. P., and Peltzer, G.: Systematic InSAR tropospheric phase delay corrections from global meteorological reanalysis data, *Geophys. Res. Lett.*, 38, 2011.
- Kouba, J.: Implementation and testing of the gridded Vienna Mapping Function 1 (VMF1), *J. Geodesy.*, 82, 193-205, 2007.
- Liao, M., Jiang, H., Wang, Y., Wang, T., and Zhang, L.: Improved topographic mapping through high-resolution SAR interferometry with atmospheric effect removal, *ISPRS. J. Photogramm.*, 80, 72-79, 2013.
- Mateus, P., Nico, G., and Catalão, J.: Can spaceborne SAR interferometry be used to study the temporal evolution of PWV?, *Atmospheric Research*, 119, 70-80, 2013a.
- Mateus, P., Nico, G., Tome, R., Catalao, J., and Miranda, P. M. A.: Experimental study on the atmospheric delay based on GPS, SAR interferometry, and numerical weather model data, *IEEE T. Geosci. Remote*, 51, 6-11, 2013b.
- Smith, E. K. and Weintraub, S.: The constants in the equation for atmospheric refractive index at radio frequencies, *Proceedings of the IRE*, 41, 1035-1037, 1953.
- Zebker, H. A., Rosen, P. A., and Hensley, S.: Atmospheric effects in interferometric synthetic aperture radar surface deformation and topographic maps, *J. Geophys. Res.*, 102, 7547-7563, 1997.



Table 1. Acquisition dates of master and slave images and their parameter information.

Number	Mater (DDMMYYYY)	Slave (DDMMYYYY)	Normal baseline (m)	Temporal baseline (days)	Height ambiguity (m)
1	06 October 2007	15 December 2007	-62.75	70	146.83
2	06 October 2007	19 January 2008	36.16	105	254.84
3	15 December 2007	19 January 2008	98.34	35	93.77
4	19 January 2008	03 May 2008	-51.85	105	177.05
5	03 May 2008	07 June 2008	217.11	35	42.54
6	03 May 2008	16 August 2008	-191.01	105	48.30
7	07 June 2008	16 August 2008	-27.67	70	333.19
8	16 August 2008	25 October 2008	31.72	70	290.90
9	16 August 2008	29 November 2008	-298.42	105	30.92
10	25 October 2008	29 November 2008	-284.21	35	32.48

Table 2. Constants used for calculating atmospheric delay

Constant	Value
$R_d$	$287.05 \text{ Jkg}^{-1}\text{K}^{-1}$
$R_v$	$461.95 \text{ Jkg}^{-1}\text{K}^{-1}$
$g_0$	$9.81 \text{ ms}^{-2}$
$k_1$	$0.776 \text{ KPa}^{-1}$
$k_2$	$0.716 \text{ KPa}^{-1}$
$k_3$	$3.75 \times 10^3 \text{ K}^2\text{Pa}^{-1}$
$\rho$	$1000 \text{ kgm}^{-3}$

- 5 Table 3. Assessment of  $\Delta\text{PWV}$  maps obtained by InSAR (master image-16 August 2008, slave image-25 October 2008). For each GPS station, PWV differences from GPS between master and slave SAR acquisition times are computed and compared



to the average values of InSAR estimates at pixels located within a circular area of 5.4 km around each GPS station. Differences are summarized in the last column. MAE and Std represent the mean absolute error and standard deviation.

Number	GPS station	Longitude (°)	Latitude (°)	$\Delta PWV_{GPS}$ (mm)	$\Delta PWV_{InSAR}$		Difference (mm)
					Mean (mm)	Std (mm)	
1	AZU1	-117.896	34.126	28.94	28.62	0.65	0.32
2	BGIS	-118.159	33.967	30.15	29.92	0.47	0.23
3	BKMS	-118.094	33.962	29.89	29.64	0.28	0.25
4	CCCO	-118.211	33.876	29.50	30.26	0.43	-0.76
5	CGDM	-117.964	34.243	25.13	27.02	1.47	-1.89
6	CNPP	-117.608	33.857	30.87	29.84	1.37	1.03
7	CVHS	-117.901	34.082	29.10	28.66	0.42	0.44
8	DYHS	-118.125	33.937	29.03	29.50	0.30	-0.47
9	ECFS	-117.411	33.647	24.51	26.03	1.22	-1.52
10	EWPP	-117.525	34.104	26.71	25.98	0.46	0.73
11	GVR5	-118.112	34.047	28.83	29.84	0.34	-1.01
12	HOLP	-118.168	33.924	29.53	29.77	0.50	-0.24
13	LBC1	-118.137	33.832	30.29	29.78	0.32	0.51
14	LBC2	-118.173	33.791	29.31	29.68	0.32	-0.37
15	LBCH	-118.203	33.787	29.22	29.62	0.37	-0.40
16	LONG	-118.003	34.111	31.31	31.23	0.35	0.08
17	LORS	-117.754	34.133	26.58	26.82	0.79	-0.24
18	MAT2	-117.436	33.856	28.24	28.35	0.87	-0.11
19	NOCO	-117.569	33.919	30.77	29.51	0.90	1.26
20	PSDM	-117.807	34.091	28.30	27.79	0.45	0.51
21	RHCL	-118.026	34.019	28.53	29.36	0.64	-0.83
22	SBCC	-117.661	33.553	30.72	30.51	0.54	0.21
23	SGDM	-117.861	34.205	27.87	27.15	1.16	0.72
24	SPMS	-117.848	33.992	28.14	28.56	0.51	-0.42
25	VYAS	-117.992	34.030	30.39	29.24	0.52	1.15
26	WCHS	-117.911	34.061	30.38	29.74	0.44	0.64
27	WHC1	-118.031	33.979	29.66	29.21	0.64	0.45
28	WLSN	-118.055	34.226	18.08	20.92	1.61	-2.84
29	WNRA	-118.059	34.043	30.34	29.68	0.45	0.66



MAE	0.70
Std	0.96

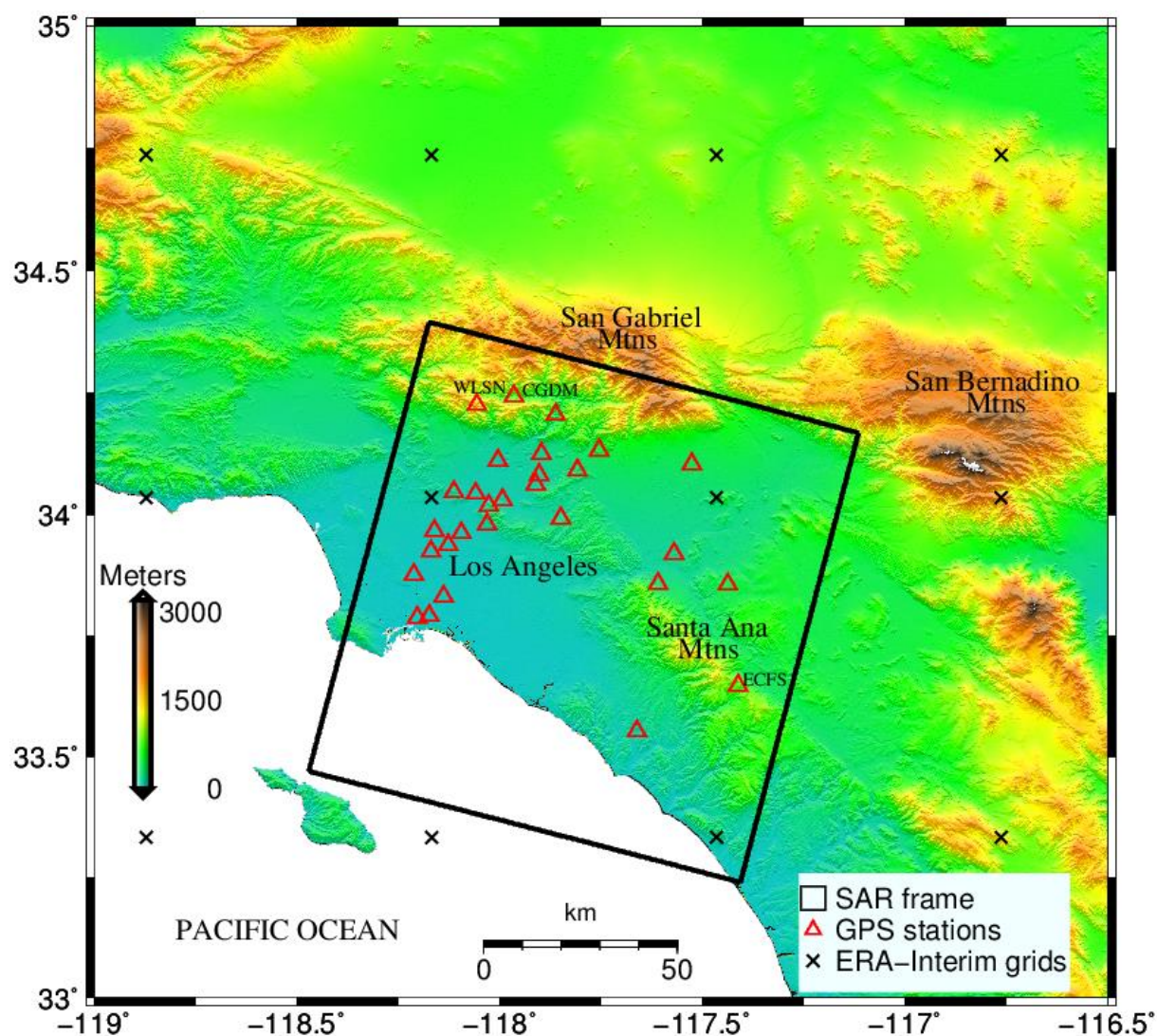


Figure 1. The topography map of the study area. The red triangles represent the locations of GPS stations. The locations of  
 5 GPS stations CGDM, ECFS, and WLSN are indicated. The black box indicate the footprint of ENVISAT ASAR images.  
 Black crosses indicate the position of the ERA-Interim model grid nodes used in this study.

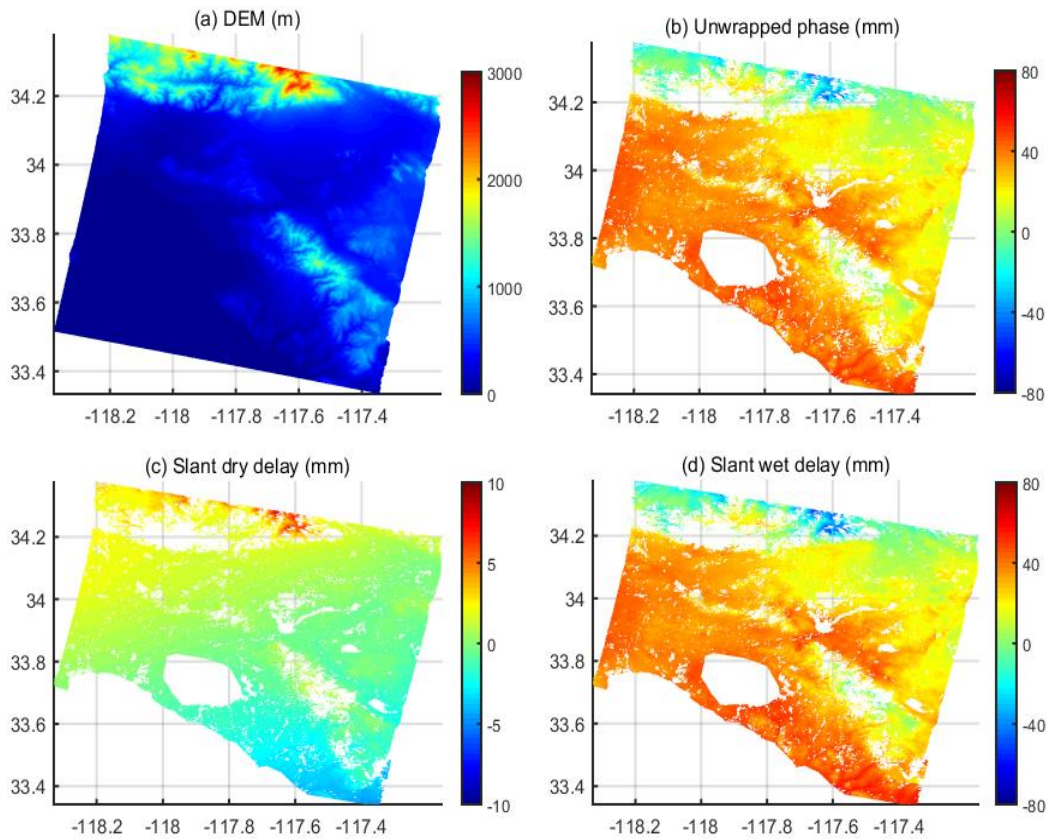


Figure 2. (a) Regional land topography from SRTM, re-sampled to radar coordinate. (b) Unwrapped phase of differential interferogram (master image-16 August 2008, slave image-25 October 2008). (c) Slant dry delay maps predicted from ERA-Interim. (d) Slant wet delay obtained by subtracting (c) from (b). The rapidly subsiding areas are masked out and significant decorrelation pixels are dropped in (b), (c), and (d).

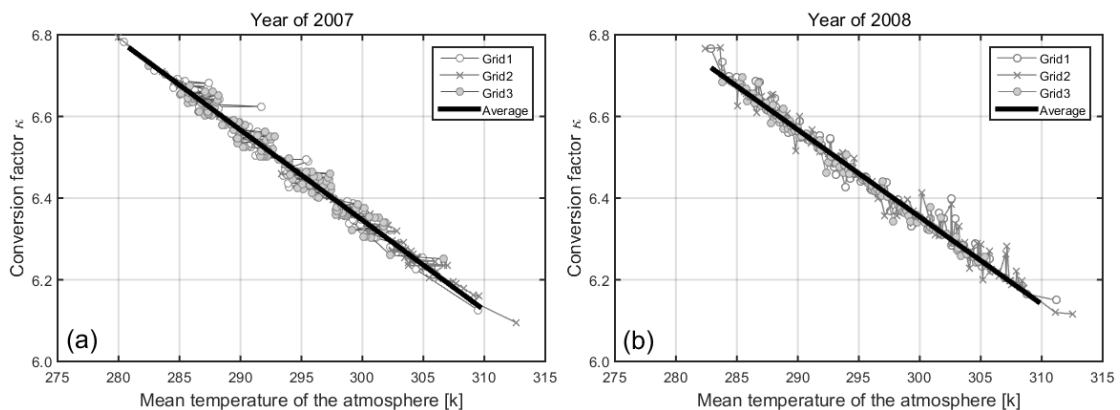




Figure 3. Conversion factor  $\kappa$  estimated based on the water vapor partial pressure and temperature extracted at three ERA-Interim model grids located within the SAR scene (see Fig. 1). The black line is the linear regression between the average of conversion factors and the mean temperature. The measurements were taken at 18:00 (closest to the SAR acquisition time) over 120 days (10 days/month) in the year 2007 (a) and 2008 (b).

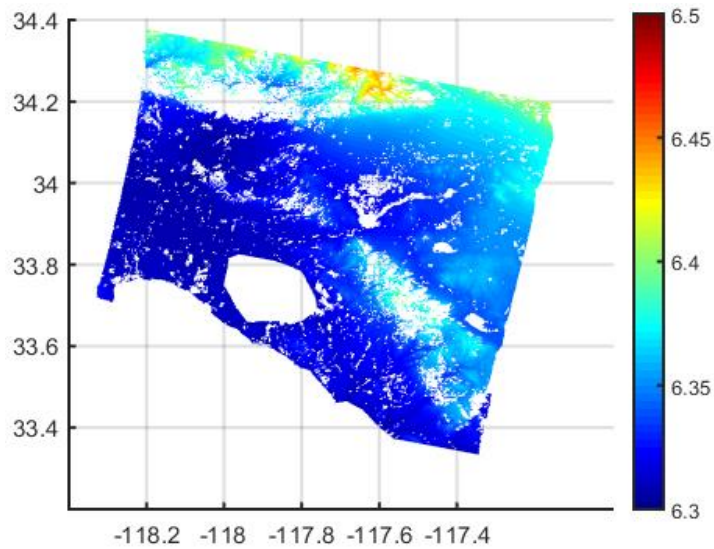


Figure 4. The spatial distribution of conversion factor  $\kappa$  calculated based on ERA-Interim. It is calculated at the time 18:00 UTC on 16 August 2008.

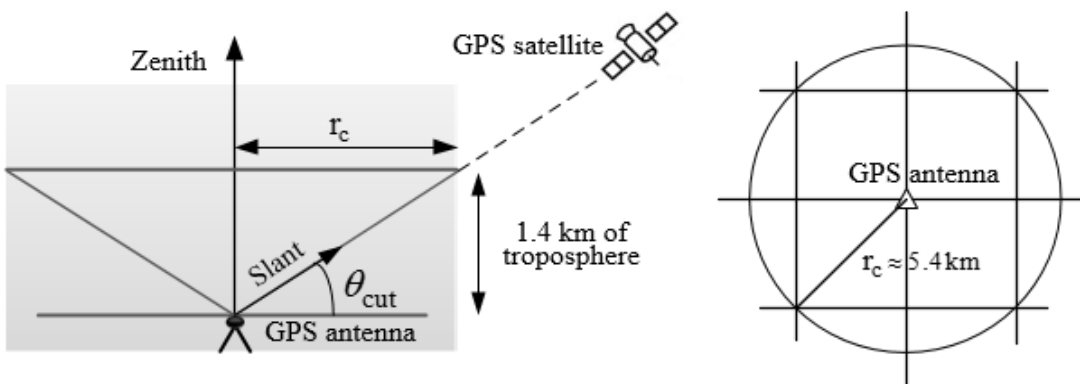
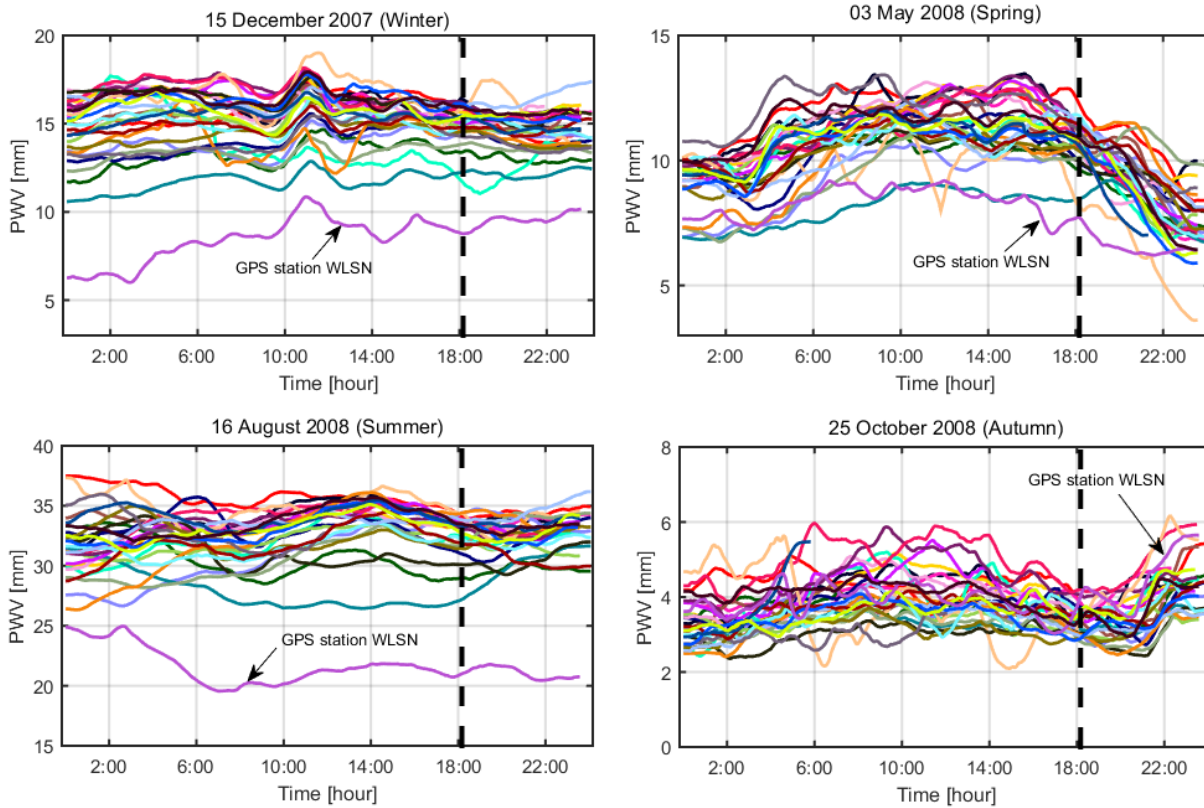




Figure 5. GPS receiver records a satellite signal at a cutoff elevation angle  $\theta_{\text{cut}}$  defining a cone-like tropospheric section above the antenna. For  $\theta_{\text{cut}} = 15^\circ$ ,  $r_c \approx 5.4 \text{ km}$ . The  $\Delta\text{PWV}$  estimated by InSAR pixels within this circle are averaged to emulate GPS-based  $\Delta\text{PWV}$ .



5

Figure 6. 24-hour time series of PWV estimated from GPS observations at 29 GPS stations located in the study area (as shown in Fig. 1) on four SAR acquisition dates. The vertical black dashed lines represent the SAR satellite overpass time (18:01 UTC). Black arrows in each plot indicate the location of GPS station WLSN (a litude about 1700) on Mount Wilson.

10 In general, the higher GPS station is, the lower the PWV value.

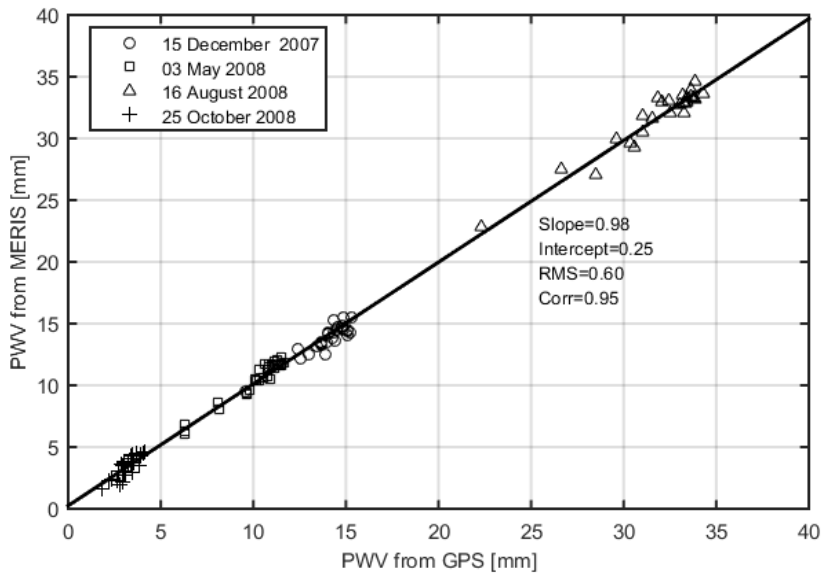


Figure.7 MERIS PWV against GPS PWV at 29 stations on four days of ENVISAT overpass time. The MERIS observations are averaged within circles of 5.4 km radius centered on the GPS station.

5

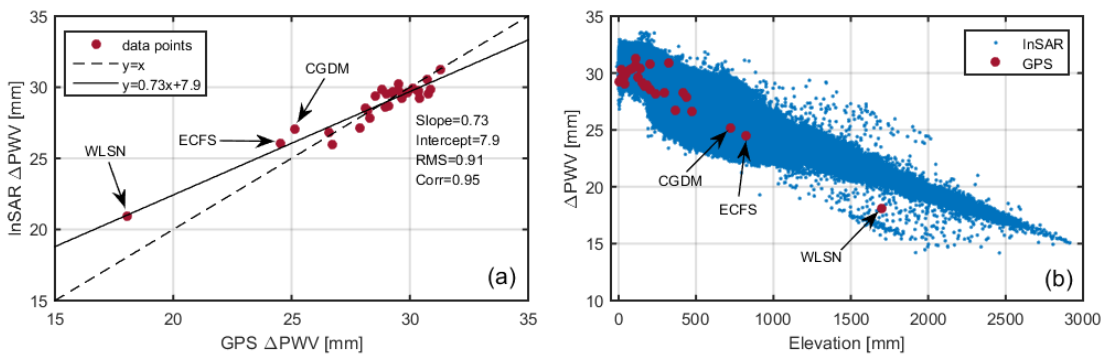
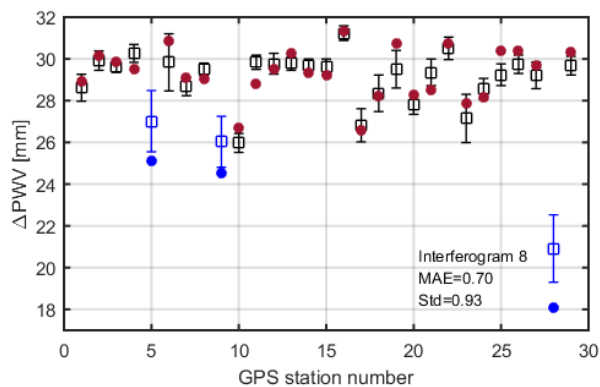
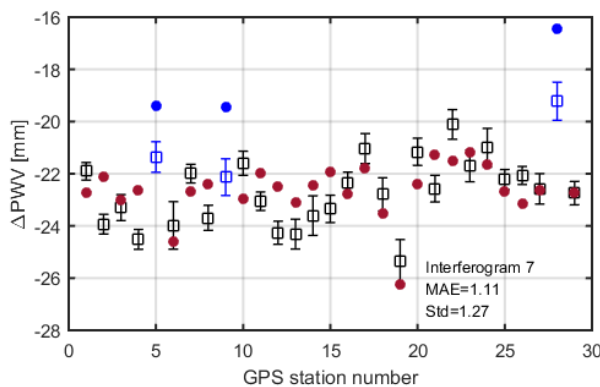
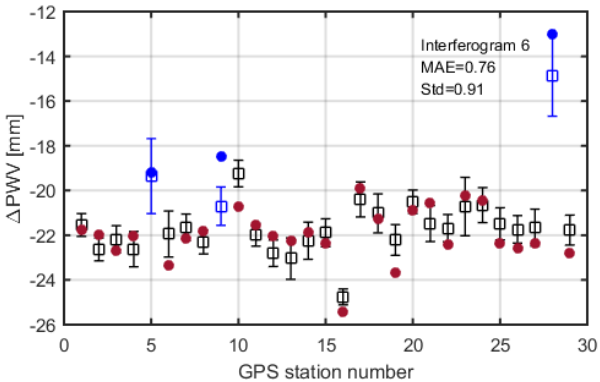
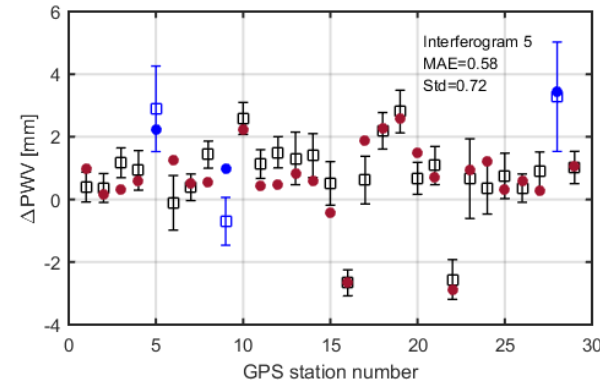
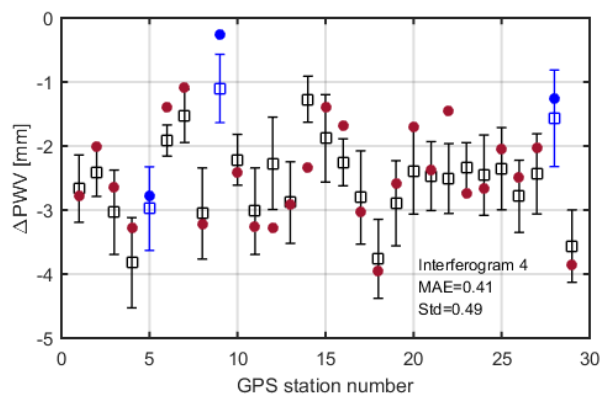
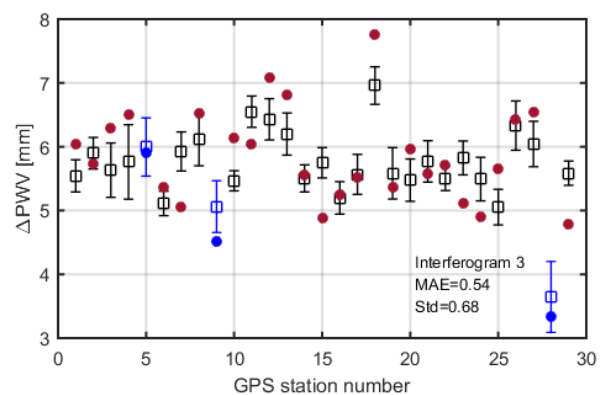
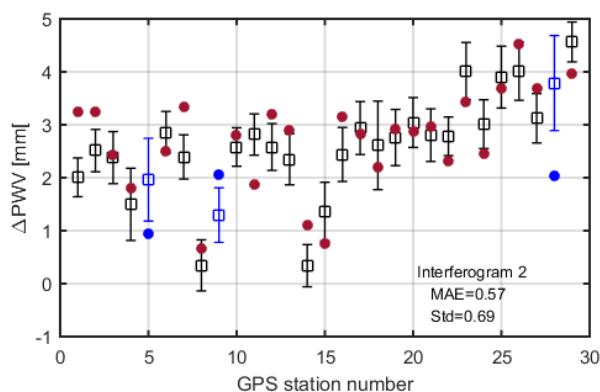
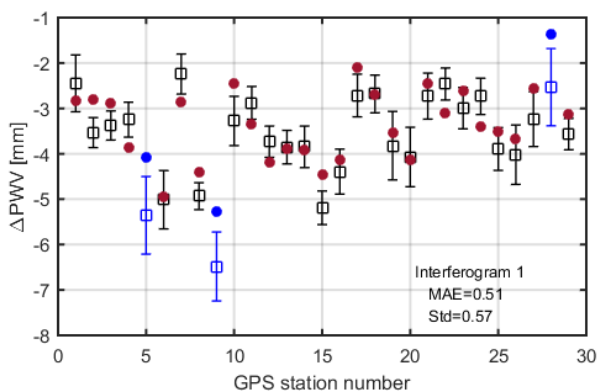


Figure 8. (a) GPS  $\Delta$ PWV plotted against the calibrated  $\Delta$ PWV from the interferogram (master image-16 August 2008, slave image-25 October 2008). The slope of the solid line in the figure is 0.73, large differences were found on stations CGDM, ECFS, and WLSN. (b) GPS (red) and InSAR (blue)  $\Delta$ PWV plotted as a function of elevation. Black arrows indicate the location of GPS sites CGDM, ECFS, and WLSN.



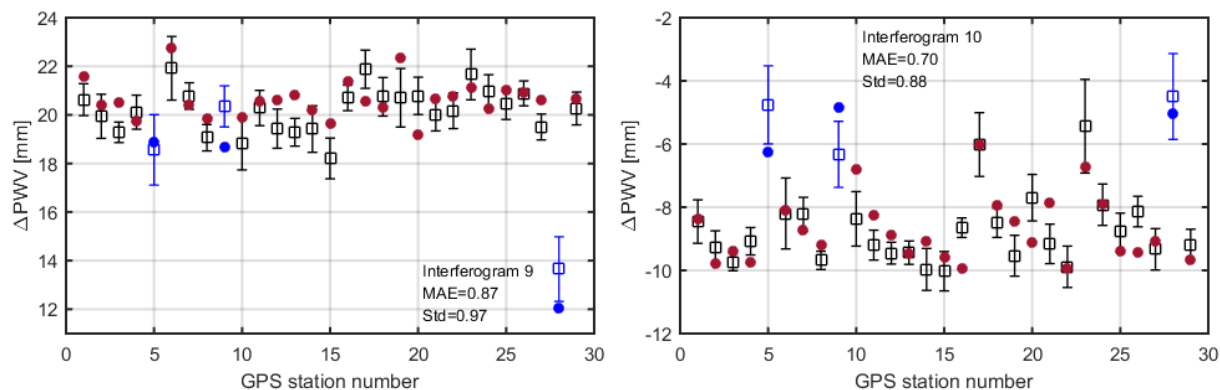
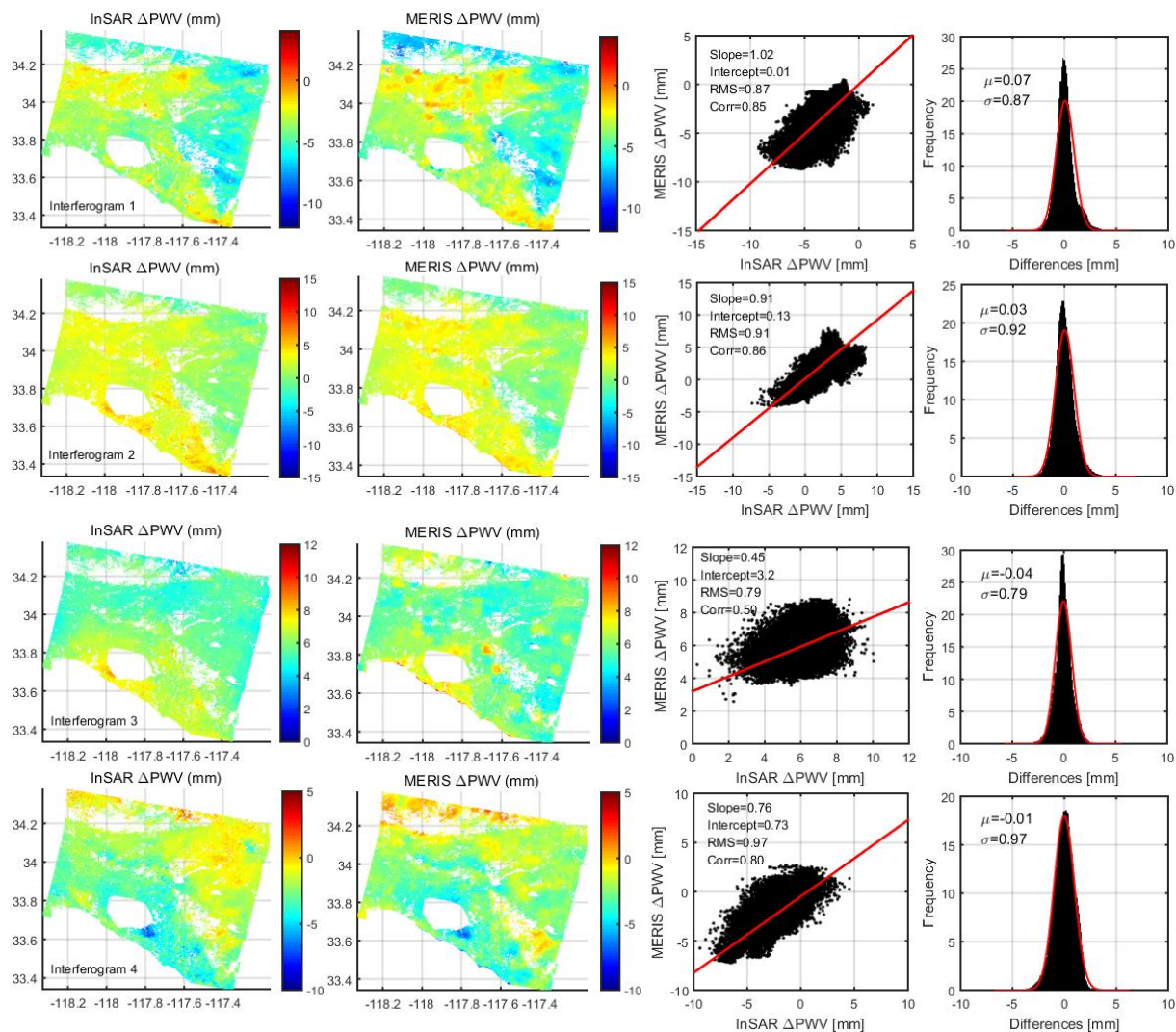
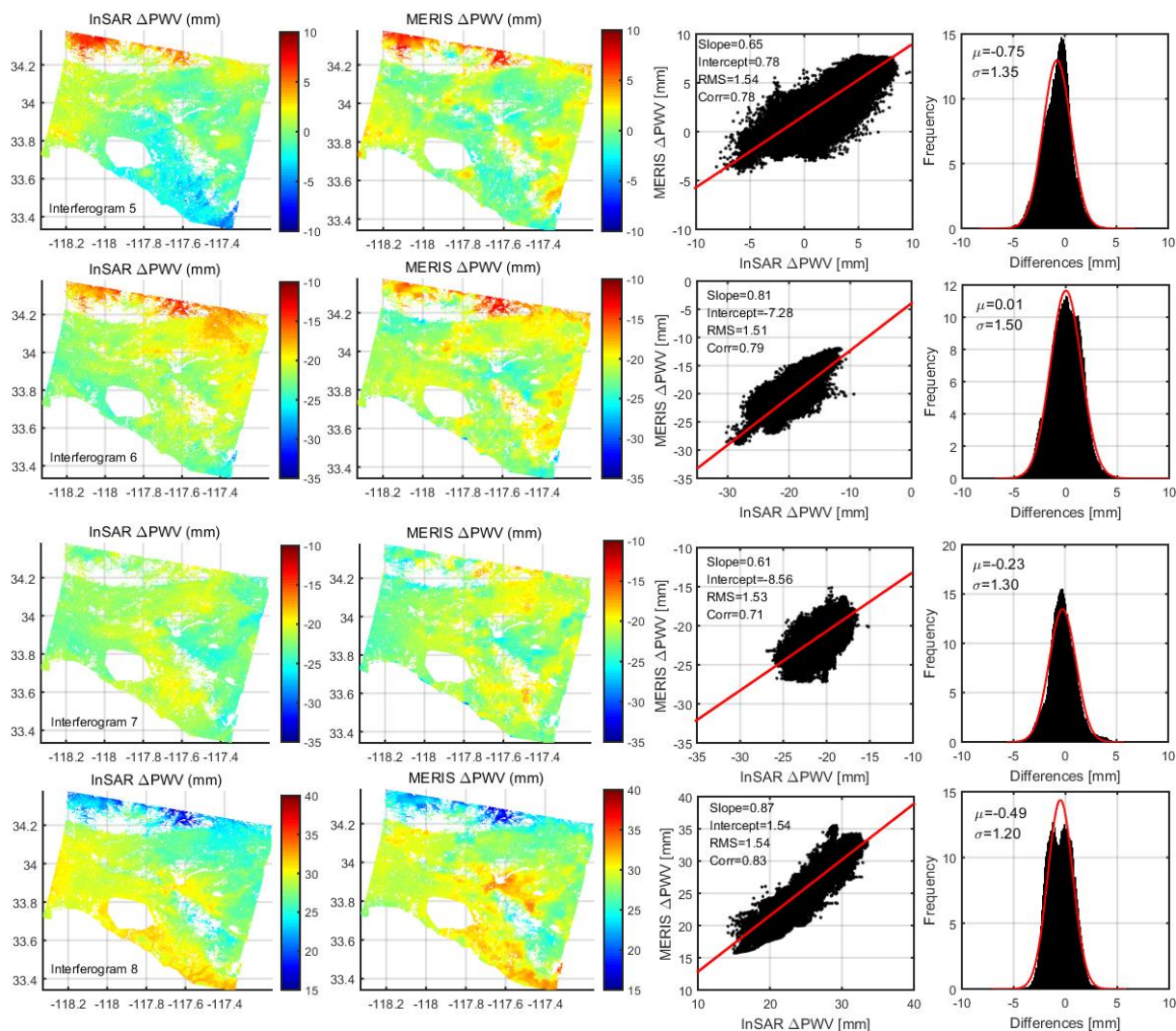


Figure 9. Comparisons of  $\Delta PWV$  estimates from InSAR (squares) and collocated GPS measurements for each GPS station (circles). The InSAR  $\Delta PWV$  are estimated from the ten interferograms in Table 1. The squares indicate  $\Delta PWV$  estimates from InSAR that are obtained by averaging all pixels falling within the circular area with a radius of 5.4 km centered around the station, corresponding to the observational cone above the GPS receiver. The error bars denote standard deviation of the pixel values in the circular area. The blue color in each plot (from left to right) represent the GPS stations CGDM, ECFS and WLSN, respectively.





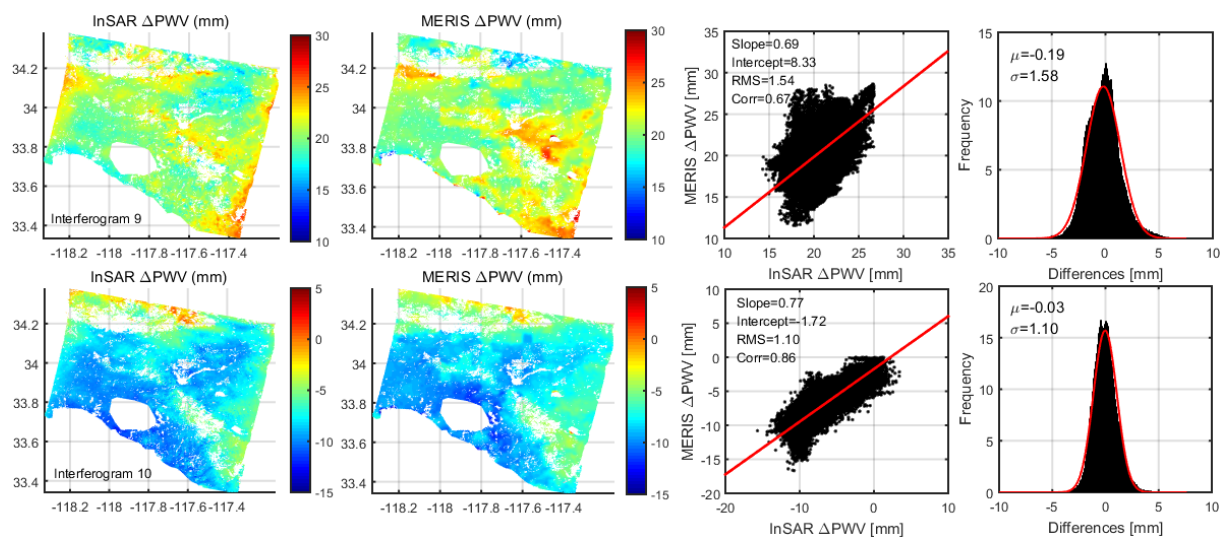


Figure 10. Comparison of the  $\Delta$ PWV maps derived from InSAR and MERIS. For all images here, the root mean square (RMS), correlation (Corr), differential mean ( $\mu$ ), and standard deviation ( $\sigma$ ) are computed.